Materials Today Bio 26 (2024) 101018

Contents lists available at ScienceDirect

Materials Today Bio

journal homepage: www.journals.elsevier.com/materials-today-bio

Mn-phenolic networks as synergistic carrier for STING agonists in tumor immunotherapy

Yingcai Meng [a,b,1], Jiaxin Huang [a,1], Jinsong Ding [a], Haiyan Zhou [c,d,**], Yong Li [e,***], Wenhu Zhou [a,*]

[a] Xiangya School of Pharmaceutical Sciences, Central South University, Changsha 410013, Hunan, China
[b] Xiangya Hospital, Central South University, Changsha 410008, Hunan, China
[c] Department of Pathology, School of Basic Medicine, Central South University, China
[d] Department of Pathology, Xiangya Hospital, Central South University, China
[e] Department of Pediatric Surgery, Hunan Children's Hospital, Changsha 410004, Hunan, China

ARTICLE INFO

Keywords:
STING pathway
Drug delivery
Immunomodulation
Tumor microenvironment

ABSTRACT

The cGAS-STING pathway holds tremendous potential as a regulator of immune responses, offering a means to reshape the tumor microenvironment and enhance tumor immunotherapy. Despite the emergence of STING agonists, their clinical viability is hampered by stability and delivery challenges, as well as variations in STING expression within tumors. In this study, we present Mn-phenolic networks as a novel carrier for ADU-S100, a hydrophilic STING agonist, aimed at bolstering immunotherapy. These nanoparticles, termed TMA NMs, are synthesized through the coordination of tannic acid and manganese ions, with surface modification involving bovine serum albumin to enhance their colloidal stability. TMA NMs exhibit pH/GSH-responsive disintegration properties, enabling precise drug release. This effectively addresses drug stability issues and facilitates efficient intracellular drug delivery. Importantly, TMA NMs synergistically enhance the effects of ADU-S100 through the concurrent release of Mn^{2+}, which serves as a sensitizer of the STING pathway, resulting in significant STING pathway activation. Upon systemic administration, these nanoparticles efficiently accumulate within tumors. The activation of STING pathways not only induces immunogenic cell death (ICD) in tumor cells but also orchestrates systemic remodeling of the immunosuppressive microenvironment. This includes the promotion of cytokine release, dendritic cell maturation, and T cell infiltration, leading to pronounced suppression of tumor growth. Combining with the excellent biocompatibility and biodegradability, this Mn-based nanocarrier represents a promising strategy for enhancing tumor immunotherapy through the cGAS-STING pathway.

1. Introduction

Tumor immunotherapy represents a promising strategy for combatting cancer by harnessing the body's immune system to selectively target and eliminate malignant cells. Despite the availability of various immunotherapeutic agents, the overall response rate remains limited, hovering at approximately 30% [1,2]. This restrained efficacy can be attributed to the formidable obstacle of the immunosuppressive microenvironment that pervades tumors. Within this hostile milieu, a multitude of factors, including immune checkpoint molecules, immunosuppressive cell populations, and soluble mediators, collectively conspire to subdue immune responses against cancer cells [3–7]. Consequently, the immunosuppressive landscape within tumors significantly compromises the potency of immunotherapy.

Researchers are diligently exploring diverse approaches to restructure the tumor microenvironment with the aim of bolstering the effectiveness of tumor immunotherapy [8–10]. One particularly promising avenue centers on the cyclic GMP-AMP synthase (cGAS)-stimulator of interferon genes (STING) pathway [11,12]. This innate immune signaling cascade responds to cytosolic DNA and triggers the production

* Corresponding author.
** Corresponding author.
*** Corresponding author.
E-mail addresses: yanhaizhou78@163.com (H. Zhou), liyongpuwaike@163.com (Y. Li), zhouwenhuyaoji@163.com (W. Zhou).
[1] These authors contributed equally to this work.

https://doi.org/10.1016/j.mtbio.2024.101018
Received 11 December 2023; Received in revised form 21 February 2024; Accepted 5 March 2024
Available online 11 March 2024

of type I interferons and pro-inflammatory cytokines [13–15]. These cytokines possess the capacity to modulate various facets of the cancer immunity cycle, encompassing antigen release and presentation, as well as the recruitment and infiltration of T cells [16–19]. Activation of the STING pathway, therefore, holds the potential to generate a pro-inflammatory milieu within the tumor microenvironment, countering its intrinsic immunosuppressive attributes. The development of STING agonists that can foster a more favorable immune milieu is a key objective in the pursuit of enhanced tumor immunotherapy.

As the understanding of STING's structure and mechanisms advances, a myriad of STING agonists have emerged, encompassing natural and synthetic cyclic dinucleotides (CDNs) as well as non-CDNs [18, 20–22]. Among these, ADU-S100, the first CDN STING agonist to advance into clinical trials for cancer therapy, has demonstrated noteworthy efficacy in restraining tumor growth and curtailing metastasis in murine models [23–25]. Presently, ADU-S100 is undergoing phase I/II clinical trials for treating advanced metastatic solid tumors and lymphomas [26–28]. Nonetheless, ADU-S100 confronts several challenges, including issues related to stability, negative charge-associated impediments to effective cellular targeting, inefficient cytoplasmic transport, and heightened hydrophilicity [18,23,29–31]. Consequently, the predominant mode of ADU-S100 administration remains intratumoral delivery. Thus, there exists an urgent imperative to formulate innovative strategies aimed at enhancing the pharmacological attributes of ADU-S100, with a view to elevating therapeutic efficacy while mitigating adverse effects.

Another pivotal consideration is the expression of STING within tumor cells. Studies have revealed that STING expression is frequently downregulated in clinical cancer tissues, particularly in advanced tumor stages [32,33]. This diminishment in STING expression is often correlated with a poorer prognosis, as tumors exhibiting low STING expression tend to mount feeble responses to STING agonists, culminating in diminished therapeutic efficacy. Consequently, enhancing the responsiveness of tumor cells to STING agonists emerges as a critical objective for optimizing therapeutic outcomes. Encouragingly, recent investigations have underscored the role of manganese in activating the cGAS-STING pathway [34]. These studies have demonstrated that manganese can directly activate cGAS, inducing a conformational shift that triggers STING pathway activation [35]. This event enhances the binding affinity between STING agonists and STING [36], suggesting that manganese could serve as a sensitizer, amplifying the activation of STING agonists for superior immunotherapeutic outcomes.

Inspired by these insights, the present study introduces Mn-phenolic networks (TM NMs) as a versatile carrier for the delivery of ADU-S100, with the ultimate goal of enhancing immunotherapy (Scheme 1). By capitalizing on tannic acid (TA), an FDA-approved biodegradable polyphenolic compound, as a ligand for coordinating with Mn^{2+}, we have crafted TM NMs. These nanoparticles efficiently encapsulate ADU-S100 through the synergistic interplay of coordination and hydrogen bonding interactions. After surface modification with bovine serum albumin (BSA), the resulting nanoparticles (TMA NMs) hold high colloidal stability under physiological conditions, facilitating effective delivery and cellular uptake. Simultaneously, it permits the rapid release of the therapeutic payload in response to intracellular cues, such as acidic pH and glutathione (GSH). The amalgamation of ADU-S100 and Mn^{2+} leads to robust activation of the STING pathway within tumor cells. Remarkably, this STING activation within tumor cells triggers immunogenic apoptosis, characterized by the liberation of damage-associated molecular patterns (DAMPs) and antigens, thereby classifying it as immunogenic cell death (ICD). Concomitantly, STING pathway activation exerts a profound immune-stimulatory influence, resulting in the heightened release of a diverse array of cytokines and chemokines. The collective effect of these factors precipitates a substantial transformation of the tumor microenvironment, typified by the activation and maturation of dendritic cells (DCs) and the infiltration of cytotoxic T cells. This transformative outcome translates into marked suppression of tumor growth following systemic nanoparticle administration, underscored by the high biocompatibility of this Mn-phenolic nanocarrier.

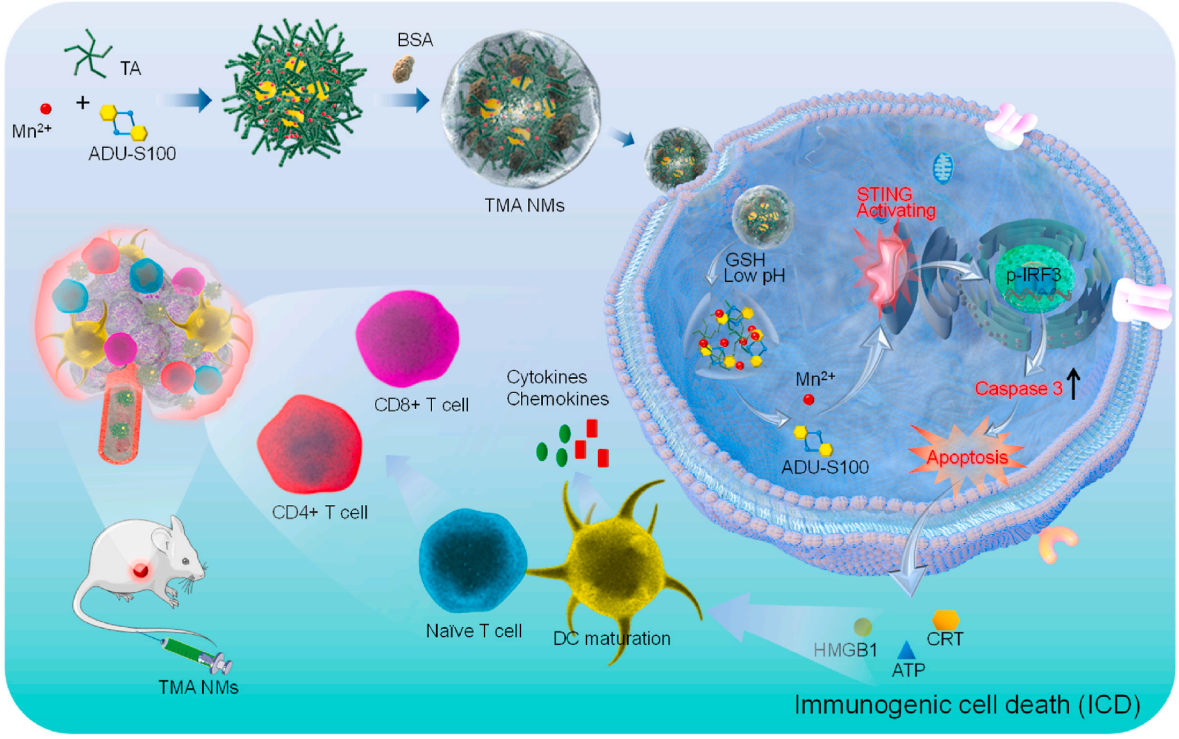

Scheme 1. Schematic illustrating the preparation of TMA NMs and the anti-tumor mechanisms. The co-release of ADU-S100 and Mn^{2+} inside cells led to significant activation of the STING pathway. This STING activation triggered immunogenic apoptosis and systemic remodeling of tumor microenvironment, which collectively contribute to enhanced tumor immunotherapy.

With its straightforward, environmentally responsible synthesis and remarkable capacity for drug loading, these Mn-phenolic networks emerge as a promising solution for the delivery of STING agonists, which is superior to other carriers [37–41]. Beyond addressing delivery challenges, these nanosystems also enhance the activity of STING agonists, promising to invigorate immunotherapy through the cGAS-STING pathway.

2. Materials and methods

2.1. Materials

The manganese chloride tetrahydrate ($MnCl_2{\cdot}4H_2O$), tannic acid (TA), 3-[4,5-dimethylthiazol-2-yl]-2,5-diphenyl tetrazolium bromide (MTT) and Dimethyl sulfoxide (DMSO) were purchased from Sigma-Aldrich (St Louis, MO, USA). The 4-(2-hydroxyethyl) piperazine-1-ethanesulfonic acid (HEPES) and bovine serum albumin (BSA) were purchased from BioFroxx (Einhausen, Germany). The ADU-S100 ammonium salt was provided by MedChemExpress. The HPLC grade acetonitrile, acetic acid and triethylamine were obtained from Anaqua Chemicals Supply (DE, USA). RPMI-1640 cell culturing medium and FBS were bought from Gibco (Grand Island, NY, USA). Penicillin–streptomycin solution and 0.25% (w/v) trypsin solution were obtained from Solarbio Biotech, Co., Ltd (Beijing, China). The Caspase-3 Assay Kit (Magic Red) and Hoechst 33342 were provided by Abcam Plc (London, UK). The Cy5.5/Cy7 modified BSA, FITC-conjugated anti-CRT antibody and Dil were purchased from Bioss Antibodies (MA, USA). Annexin V-FITC/PI apoptosis kit was provided from Multisciences Biotech (Hangzhou, China). The Enhanced ATP Assay Kit was purchased from Beyotime Technology (Shanghai, China). The antibody against phospho-STING and HMGB1 were purchased from Proteintech Group (Wuhan, China). The antibody against phospho-IRF3 was obtained from ABclonal Technology Co., Ltd. (Wuhan, China). The RIPA lysis buffer, antibody against GAPDH and HRP-conjugated secondary antibodies were obtained from Biosharp (Hefei, China). The antibody against β-Tublin was provided by Zen-Bioscience Co., Ltd. (Chengdu, China). TRAzol reagent and qPCR mix were purchased from Dongsheng Biotech (Guangzhou, China) and Transgene Biotech (Beijing, China), and the cDNA reverse transcription kit was purchased from Invitrogen (Carlsbad, CA). The Cytokines ELISA kits and the primers (HPLC purification) of IFN-β, IL-6, CXCL10, TNF-α and GAPDH were obtained from Sangon Biotech (Shanghai, China). The primer sequences were listed in Table 1. The ELISA kits of alanine aminotransferase (ALT), aspartate aminotransferase (AST), creatinine (Cre), blood urea nitrogen (BUN), and creatine kinase isoenzymes (CK-MB) were purchased from Jiancheng Bioengineering Institute (Nanjing, China).

2.2. Cells culture and animals

The mouse breast cancer cells (4T1 cells) were provided from Xiangya Cells Center (Changsha, China), and were cultured and grown in RPMI 1640 with 10% FBS and 1% streptomycin/penicillin in a humidified atmosphere with 5% CO_2 at 37 °C. The BALB/c mice were purchased from Hunan SJA Laboratory Animal CO., LTD (Hunan, China). All the animal experiments were performed in accordance with the Regulations for the Administration of Affairs Concerning Experimental Animals of China, and approved by the Ethics Committee for Research in Animal Subjects at Xiangya School of Pharmaceutical Sciences of Central South University.

Table 1
The primer sequences used in qPCR.

Gene	Foword primer (5'→3')	Reverse primer (5'→3')
IFN-β	CTGGGTGGAATGAGACTATTGT	AAGTTCCTGAAGATCTCTGCTC
IL-6	CAAAGCCAGAGTCCTTCAGAG	GTCCTTAGCCACTCCTTCTG
CXCL10	CAACTGCATCCATATCGATGAC	GATTCCGGATTCAGACATCTCT
TNF-α	ATGTCTCAGCCTCTTCTCATTC	GCTTGTCACTCGAATTTTGAGA
GAPDH	GGGTCCCAGCTTAGGTTCAT	CCAATACGGCCAAATCCGTT

2.3. Preparation of TM NMs

Briefly, 22.5 μL, 40 mg/mL TA and 100 μL, 100 mM, pH 7.4 HEPES were sequentially added into 850 μL ddH_2O, rapidly added 25 μL, 10 mg/mL $MnCl_2$, followed by 5 min vigorous stir. Then, slowly added 750 μL previous mixture into 375 μL BSA solution (containing 225 μL H_2O, 100 μL, 10 mg/mL BSA and 50 μL, 10 mM, pH 7.4 HEPES), following addition of 125 μL, 10 mg/mL $MnCl_2$ for 40 min vigorous stir again. Finally, the nanoparticles were collected by centrifugation and dispersed in 10 mM pH 7.4 HEPES.

2.4. Preparation of TMA NMs

Briefly, 22.5 μL, 40 mg/mL TA, 100 μL, 100 μg/mL ADU-S100 and 100 μL, 100 mM, pH 7.4 HEPES were sequentially added into 750 μL ddH_2O, rapidly added 25 μL, 10 mg/mL $MnCl_2$, followed by 5 min vigorous stir. Then, slowly added 750 μL previous mixture into 375 μL BSA solution (consisting 225 μL H_2O, 100 μL, 10 mg/mL BSA and 50 μL, 10 mM, pH 7.4 HEPES), following addition of 125 μL, 10 mg/mL $MnCl_2$ for 40 min vigorous stir again. Finally, the nanoparticles were collected by centrifugation and dispersed in 10 mM pH 7.4 HEPES. Cy5.5-BSA or Cy7-BSA was coated by the same procedure to obtain Cy5.5- or Cy7-labeled nanoparticles, respectively.

2.5. Characterization of TM NMs and TMA NMs

The UV–vis absorption spectra were measured by an UV–vis spectrophotometer (UV-2600, Shimadzu). The formation and degradation of TM NMs in different pH conditions and varied concentrations of GSH were monitored by the change of UV–vis absorption spectra. The powder of $MnCl_2{\cdot}4H_2O$, TA and TA@Mn were used for the measurement of Fourier transform infrared reflection-absorption (FT-IR, Spectrum Two, PerkinElmer). The ZetaSizer Nano ZS (Malvern Instruments, UK) was used to measure the particle size and ζ potential. The stability in different media (H_2O, HEPES, and 10% FBS-containing RPMI 1640) was studied by monitoring the particle size change over time. TEM (Titan G2-F20, FEI, USA) was used to characterize the morphology and size of the nanoparticles. The powder of TMA was used for analysis of X-ray photoelectron spectroscopy (XPS, Nexsa, Thermo Fisher, MA, USA). Meanwhile, the ADU-S100 loading capacity was quantified by collecting the unloaded ADU-S100 in supernatant and measuring by high performance liquid chromatography (HPLC, Agilent 1260 Infinity II).

2.6. In vitro drug release behavior

The release behavior of Mn^{2+} and ADU-S100 from TMA NMs were examined by the centrifugation method. Briefly, TMA NMs was suspended in dissolution medium (10 mM phosphate buffer at pH 5.5 and pH 7.4). The solution was shaken in a thermostatic shaker (100 rpm, 37 °C). The release medium was sampled at predetermined time intervals and centrifuged at 16000 rpm, 10min. The ADU-S100 in supernatant was analyzed by HPLC (Agilent 1260 Infinity II). The samples of Mn^{2+} release in dissolution medium (10 mM phosphate buffer at pH 5.5, pH 7.4 and pH 7.4 plus 10 mM GSH) were obtained through above steps. The Mn content of supernatant was measured by inductively coupled plasma optical emission spectrometer (ICP-OES, SPECTRO BLUE, Germany)

2.7. GSH consumption

The GSH consumption was measured by using Reduced Glutathione (GSH) Content Assay Kit. Typically, GSH solution (10 mmol/L) was

mixed with different concentrations of TMA NMs (0, 20, 50, 100 and 200 μg/mL). After incubation for 30 min, the DTNB reagent was added and the absorbance at 412 nm was recorded for calculation of GSH consumption.

2.8. Cellular uptake assay

4T1 cells were seeded in 35 mm culture dish at a density of 5×10^4 per well and cultured overnight. Then, the cells were treated with Cy5.5 labeled TMA NMs (200 μg/mL) for 6 h. After fixing with 4% paraformaldehyde and labeling with Hoechst 33342, the cells were imaged by a confocal fluorescence microscope (LSM780 NLO, Zeiss, Oberkochen, Germany).

2.9. Cytotoxicity assay

4T1 cells were seeded in 96-well plates at a density of 5×10^3 cells per well overnight and further incubated with various concentrations of ADU-S100, TM NMs and TMA NMs for 48 h. Then, the medium was replaced by 100 μL of MTT solution (0.5 mg mL^{-1}) for 4 h incubation. Finally, the formazan crystals were dissolved in 100 μL DMSO, and the absorbance at 490 nm was measured by a microplate reader (Infinite M200 PRO, TECAN, Austria) for cell viability calculation.

2.10. Western Blotting

4T1 cells were seeded in six-well plates at a density of 4×10^5 cells per well overnight and further incubated with ADU-S100, TM NMs and TMA NMs (equivalent to ADU-S100 dose of 10 μg/mL) for 48 h. Then, 4T1 cells were scraped on ice. After centrifugation, the pellets were re-suspended in RIPA lysis buffer. The total protein concentration was determined by using BCA reagents and denatured in boiling water for 10 min. Next, equal amount of proteins were subjected to sodium dodecyl sulfate-polyacrylamide gel electrophoresis (SDS-PAGE) and transferred onto the polyvinylidene fluoride membranes. Afterward, the membranes were blocked with blocking buffer (5% BSA, 10 mM PBST) for 1 h. Then, the membranes were probed with primary antibody (against p-STING, *p*-IRF3, HMGB1, β-Tublin and GAPDH) and secondary antibodies. The protein bands were visualized by ChemiDoc XRS + system (Bio-Rad, USA).

2.11. In vitro Caspase-3 activity assessment

4T1 cells were seeded in 35 mm culture dish at a density of 2×10^4 cells per well overnight, and treated with ADU-S100, TM NMs and TMA NMs (equivalent to ADU-S100 dose of 25 μg/mL). The cellular DEVDase enzyme activity (caspase-3 activity) was detected by Caspase-3 Assay Kit (Magic Red) according to the manufacturer's protocol, and visualized using a confocal fluorescence microscope (LSM780 NLO, Zeiss, Oberkochen, Germany).

2.12. Flow cytometric analysis of apoptosis

Cell apoptosis level was evaluated by Annexin V-FITC/PI apoptosis kit according to the manufacturer's instructions. Cells were seeded in a 12-well plate at 2×10^5 cells per well and treated with various formulations for 48 h. After washing with PBS, the cells were collected and suspended in 1 × Binding Buffer. Then, 5 μL annexin V-FITC and 5 μL PI were added for flow cytometric analysis (LSRFortessa, BD, USA).

2.13. HMGB1 ELISA

4T1 cells were seeded in 12-well plates at a density of 5×10^4 cells per well overnight, and treated with different formulations for 48 h. Then, the culture medium was collected and centrifuged at 3000 rpm for 20 min, and the content of HMGB1 was measured by ELISA kits according to the standard protocol.

2.14. ATP detection assay

4T1 cells were seeded in 12-well plates at a density of 1.5×10^5 cells per well overnight, and treated with different formulations, followed by 12 h, 24 h and 48 h incubation, respectively. The extracellular ATP was measured using an Enhanced ATP Assay Kit according to the instructions.

2.15. Immunofluorescence staining of CRT

Immunofluorescence was performed to visualize the expression level of CRT on cellular membrane. 4T1 cells were seeded in 35 mm culture dish at a density of 5×10^3 per well and cultured overnight. The cells were treated with TMA NMs (equivalent to ADU-S100 dose of 10 μg/mL) for 48 h, fixed with 4% paraformaldehyde solution for 10 min, incubated with PBS (0.1% Triton-X) for 20 min, and blocked using 5% BSA for 30 min at room temperature. Then, the cells were stained with a FITC-conjugated anti-CRT antibody for 30 min at room temperature, washed three times, followed by staining with 10 μg/mL Hoechst 33342 and Dil for 30 min in cellular incubator (37 °C, 5% CO_2) to visualize the nucleus and cell surface membrane. Finally, the cells were washed three times and visualized under a confocal fluorescence microscope (LSM780 NLO, Zeiss, Oberkochen, Germany).

2.16. Hemolysis assay

The pure erythrocytes were obtained by centrifugation (3000 rpm, 10 min, 4 °C) of the whole mouse blood and washed three times by PBS. Then, 0.15 mL of 2% erythrocytes was mixed with 0.15 mL TM NMs or TMA NMs at various concentrations (15.7–250 μg/mL) for 3 h at room temperature. Then, PBS and 1% Triton X-100 were used as the negative and positive control, respectively. After centrifugation, the absorbance of the supernatant was measured at 540 nm for hemolytic analysis. Hemolytic activity (%) = $[(OD_{sample} - OD_{negative})/(OD_{positive} - OD_{negative})] \times 100\%$.

2.17. In vivo biodistribution

4T1 (1×10^6) cells were suspended in 100 μl of PBS and subcutaneously injected into the right flank region of each female BALB/c mouse to construct tumor-bearing mice, and the mice were treated with different formulations when the volume of tumors grew to ~300 mm^3. For *in vivo* fluorescence imaging, the tumor-bearing mice were injected with free Cy7 or Cy7 labeled TMA NMs intravenously at an equivalent Cy7 dose of 2.5 mg/kg. The mice were anesthetized at 12 h and 24 h post administration, respectively, and imaged with IVIS imaging system (PerkinElmer, USA). To quantify Mn accumulation, the tumors were collected at 24 h post injection of TMA NMs or equivalent amount of free Mn^{2+}, and then digested by concentrated nitric acid for ICP-MS (PerkinElmer NEXION 2000, USA) analysis. To evaluation the excretion of Mn, the main organ (including heart, liver, spleen, lung, and kidney) were collected at day 1 and day 16, and then digested by concentrated nitric acid for ICP-MS analysis.

2.18. In vivo therapeutic efficacy

The tumor-bearing mice were divided into five groups randomly (n = 5) and intravenously administrated with PBS, ADU-S100, TM NMs, TMA NMs (equivalent to ADU-S100 dose of 20 μg/kg), every other day for overall three times. The tumor volumes (0.5 × length × $width^2$) and body weight of mice were measured every other day for 16 days. On day 16, mice were sacrificed and the tumors were collected for weighting. Finally, tumors and main organs were immersed in 4% formaldehyde, followed by embedding and slicing, and the slides were stained with

hematoxylin & eosin (H&E) and observed by an optical microscope (Ti–S, Nikon, Japan).

2.19. Quantitative real-time PCR (qPCR)

After the treatments, the tumors were harvested on day 16, and homogenized using Tissuelyser-24L (Jingxin industrial development, Shanghai, China) to obtain single cell suspensions. Total RNA from tumor homogenates was isolated using the TRAzol. Total RNA (500 ng) was reverse transcribed by a SuperScript IV First-Strand Synthesis System (Thermo Fisher, MA, USA). Real-time PCR was conducted with the SYBR Green qPCR Mix or TransStart® Green qPCR SuperMix using a Bio-Rad CFX Connect Real-time System (Bio-Rad, USA). To evaluate the *in vitro* gene expression, tumor cells were treated with different formulations for 48 h. Then, the RNA was isolated and detected through above processes.

2.20. TME immune related cytokines analysis

The tumors were harvested on day 16 of the treatments, and homogenized using Tissuelyser-24L to obtain single cell suspensions. Total proteins from tumor homogenates were isolated using the RIPA lysis buffer. The levels of cytokines including IFN-β, IL-6, CXCL10 and TNF-α in tumor homogenates was determined by ELISA kits according to the instructions.

2.21. Flow cytometric analysis of immune cells

The harvested tumors were cut into small pieces, digested at 37 °C for 1 h, and filtered through 70 μm cell strainers to obtain single cell suspensions. After blocking with FcγIII/IIR-blocking Ab, the cells were stained with fluorescence-labeled antibodies at a dilution of 1:200. For macrophage re-polarization, the cells were stained with anti-CD86-Brilliant Violet 421™ (BioLegend, Clone: GL-1, Catalog: B318824) and anti-CD206-PE-CYN7 (Thermo, Clone: MR6F3, Catalog: 25-2061-82). For DCs maturation, the cells were stained with Anti-CD11c-APC/Cy7® (Abcam, Clone: 3.9, Catalog: ab272330), and anti-CD86-Brilliant Violet 421™. For T cells activation, the cells were stained with anti-CD8a-PE (BD Pharmingen, Clone: 53-6.7, Catalog: 553032), anti-CD4-Percp/Cy™5.5 (BD Pharmingen, Clone: RM4-5, Catalog: 550954) and anti–IFN–γ-FITC (BD, Clone: XMG1.2, Catalog: 554411). Afterward, the samples were analyzed by flow cytometry (FACSVerse, BD, USA).

2.22. Immunofluorescence staining

Tumor tissue was fixed in 4% paraformaldehyde, embedded in paraffin wax, and sectioned (5 μm) onto microscope slides. Caspase-3 detection was performed following the standard protocol. The images were recorded by a fluorescent microscope Nikon Ni-E (Nikon, Minato, Japan).

2.23. Biochemical index analysis

To examine the hepatic, renal and cardiac function, the levels of ALT, AST, CRE, BUN and CK-MB in the serum were determined by using the ELISA kits according to the instructions.

2.24. Statistical analysis

All the quantitative results were reported as mean ± standard deviation (SD). The T test and one-way analysis of variance (ANOVA) was used to assess the statistical significance of the different groups. The threshold of significance was defined as follows: *$p < 0.05$, **$p < 0.01$, ***$p < 0.001$, ****$p < 0.0001$.

3. Results and discussion

3.1. Preparation and characterization of TMA NMs

The synthesis of Mn-phenolic networks (TM NMs) was conducted through a coordination reaction between tannic acid (TA) and manganese ions (Mn^{2+}). To optimize this reaction, various pH conditions were employed for a 30-min incubation period. Notably, negligible color change and UV–vis absorbance were observed at pH levels below 6 (Fig. 1A). The transition from pH 6 to 9 induced a discernible darkening of the reaction solution, accompanied by the emergence of a UV–vis absorption peak. Consequently, the formation of Mn-phenolic networks was favored under alkaline conditions, while the protonation of phenolic hydroxyl groups at lower pH values led to weak coordination affinity with Mn^{2+} [42]. This coordination binding was further corroborated by Fourier-transform infrared (FT-IR) spectra, wherein characteristic peaks of TA exhibited attenuation or disappearance upon metal coordination (Fig. 1B). In the pH range of 7–9, the Mn-phenolic networks exhibited the propensity to form nanoparticles with a uniform size of approximately 150 nm (Fig. 1C). However, these nanoparticles exhibited instability and rapid aggregation within a span of 20 h (Fig. 1D), likely attributed to inadequate surface stabilization. Addressing this concern, the incorporation of bovine serum albumin (BSA) onto the particle surface was undertaken, yielding a slight increase in particle size (~250 nm) alongside significantly enhanced nanoparticle stability (fig. S1, Fig. 1E). Intriguingly, the UV–Vis absorbance of the nanoparticles notably diminished with decreasing pH or escalating glutathione (GSH) concentration (Fig. 1F and G). This observation underscores the pH/GSH-responsive disintegration of the nanoparticles, a dual-responsive property valuable for drug delivery systems, enabling targeted drug release in response to intracellular stimuli within tumor cells.

Subsequently, TM NMs were harnessed as carriers for the loading of ADU-S100, a hydrophilic STING agonist. This loading process was achieved by co-incubating TA, Mn^{2+}, and the drug under neutral pH conditions, followed by surface coating with BSA. The resultant nanoparticles, denoted as TMA NMs, exhibited a negative surface charge (−12 mV) and measured approximately 260 nm in diameter (Fig. 1H). Transmission electron microscopy (TEM) revealed the irregular morphological features characteristic of coordination polymers (Fig. 1I). UV spectroscopy discerned a pronounced absorbance peak of ADU-S100 around ~255 nm, indicative of successful drug loading (Fig. 1J). Elemental composition analysis via X-ray photoelectron spectroscopy (XPS) demonstrated discernible signals of Mn and P within the structure, providing evidence of metal coordination for ADU-S100 encapsulation (Fig. 1K-M). The integration of surface-coated BSA endowed TMA NMs with robust colloidal stability across diverse buffer conditions, affirming their utility within biological contexts (Fig. 1N).

Motivated by the nanoparticles responsiveness to environmental cues, investigations into their drug release profiles were undertaken under varied conditions. Under physiological pH (7.4), the nanoparticles exhibited a typical sustained drug release profile. Conversely, at a lowered pH of 5.5, a markedly accelerated drug release was observed, concomitant with the collapse of the coordination structure, as evidenced by the liberation of free Mn^{2+} (Fig. 1O, fig. S2). This outcome aligns with prior observations. Intriguingly, the collapse rate was further heightened upon the introduction of GSH (fig. S2). This enhanced Mn^{2+} release can be attributed to the competitive coordination of Mn^{2+} with –SH moieties within GSH, along with the –SH-mediated reaction with TA [43]. To validate this hypothesis, the consumption of GSH was quantified, revealing a direct correlation between NPs concentration and GSH utilization (Fig. 1P), underscoring the interplay between TA and GSH in the collapse of the nanoparticles.

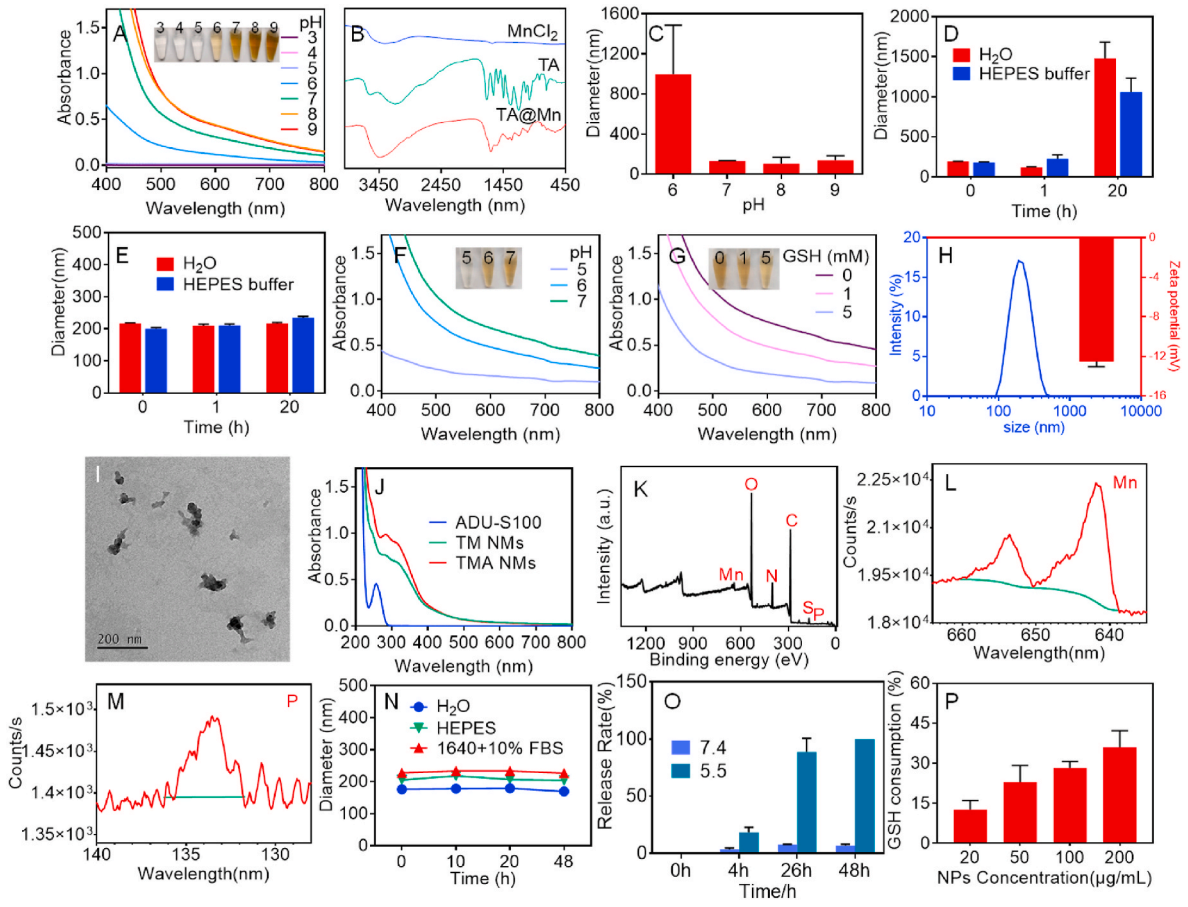

Fig. 1. (A) Appearance and UV spectra of the coordination mixture between TA and Mn^{2+} (TA@Mn) under varying pH conditions. (B) Infrared spectra depicting Mn^{2+}, TA, and TA@Mn. (C) Diameter distribution of TA@Mn synthesized across different pH conditions. Colloidal stability evaluation of TM NMs (D) without or (E) with immobilized BSA. UV–vis absorption spectra of TM NMs after incubation (F) under diverse pH conditions or (G) with varying GSH concentrations for 1 h. (H) Particle size distribution and zeta potential of TMA NMs. (I) TEM micrograph portraying the morphology of TMA NMs. (J) UV–vis absorption spectra of ADU-S100, TM NMs, and TMA NMs. (K) XPS spectra of TMA NMs with detailed enlargement of (L) Mn and (M) P peaks. (N) Colloidal stability evaluation of TMA NMs in water, HEPES buffer, and 1640 culture medium containing 10% FBS. (O) ADU-S100 release profile from TMA NMs under diverse conditions. (P) Consumption of GSH by TMA NMs.

3.2. In vitro anti-tumor effect of TMA NMs via STING pathway activation to induce tumor cells ICD

After confirming the structural integrity and essential characteristics of the nanoparticles, we proceeded to investigate the intracellular behavior of TMA NMs using murine breast cancer cells (4T1) as a model system. To facilitate cell localization, TMA NMs were initially labeled with the Cy5.5 fluorophore and subsequently co-incubated with the cells. Following a 6-h incubation period, Hoeschst 33342 was employed to label cell nuclei for precise cellular localization. Confocal laser scanning microscopy (CLSM) imaging revealed pronounced red fluorescence emitted from Cy5.5-TMA NMs-treated cells, while control cells exhibited no such fluorescence, indicative of effective cellular internalization of the nanoparticles (fig. S3).

Subsequently, we gauged the cytotoxic impact of the nanosystem via MTT assay. As a benchmark, free ADU-S100 was initially evaluated. After a 48-h incubation, it became evident that nearly 70% of cells remained viable even at concentrations as high as 500 μg/mL (Fig. 2A), underscoring the limited effect on cellular growth. This observed low cytotoxicity can be attributed to the high hydrophilicity and electronegativity of ADU-S100, which, in turn, curtailed its intracellular translocation, thus limiting its efficacy. Contrastingly, upon incubation with TM NMs, a marked cytotoxicity manifested at a concentration of 250 μg/mL (Fig. 2B). Multiple mechanisms, including Mn^{2+}-induced chemodynamic effects, STING pathway activation via Mn^{2+} [44–46], and intracellular GSH consumption, could potentially underlie the observed anti-tumor effects of these Mn-phenolic networks (figs. S4 and S5). Remarkably, in comparison with TM NMs, TMA NMs exhibited significantly elevated cytotoxicity, translating to a 3-fold decrease in the IC_{50} value (Fig. 2C and D), and this toxicity was lower for normal cells (fig. S6). We attribute this enhancement to the internalization-facilitated uptake of ADU-S100 by the nanoparticles and the synergistic STING pathway activation derived from the combined presence of Mn^{2+} and ADU-S100.

To corroborate this mechanism, we proceeded to explore the activation of the STING pathway through western blot analysis of cellular p-STING protein levels, a hallmark of STING activation. Notably, while ADU-S100 treatment induced a modest elevation in p-STING expression, indicative of STING pathway activation (Fig. 2E), TM NMs-treated cells also exhibited a measurable level of STING activation, presumably attributed to the release of Mn^{2+}. Encouragingly, TMA NMs demonstrated the most potent STING activation, as evidenced by the highest p-STING expression level, which was confirmed by the expression of *p*-IRF3 (fig. S7). It is pertinent to note that STING pathway activation prompts the release of various cytokines, including IFN-β, IL-6, CXCL10, and TNF-α (Fig. 2F–I), which can effectuate anti-tumor effects by directly damaging tumor cells or indirectly fostering anti-tumor immune responses. In concordance with this, the application of TMA NMs led to a notable increase in the levels of all these cytokines, collectively contributing to enhanced anti-tumor potential.

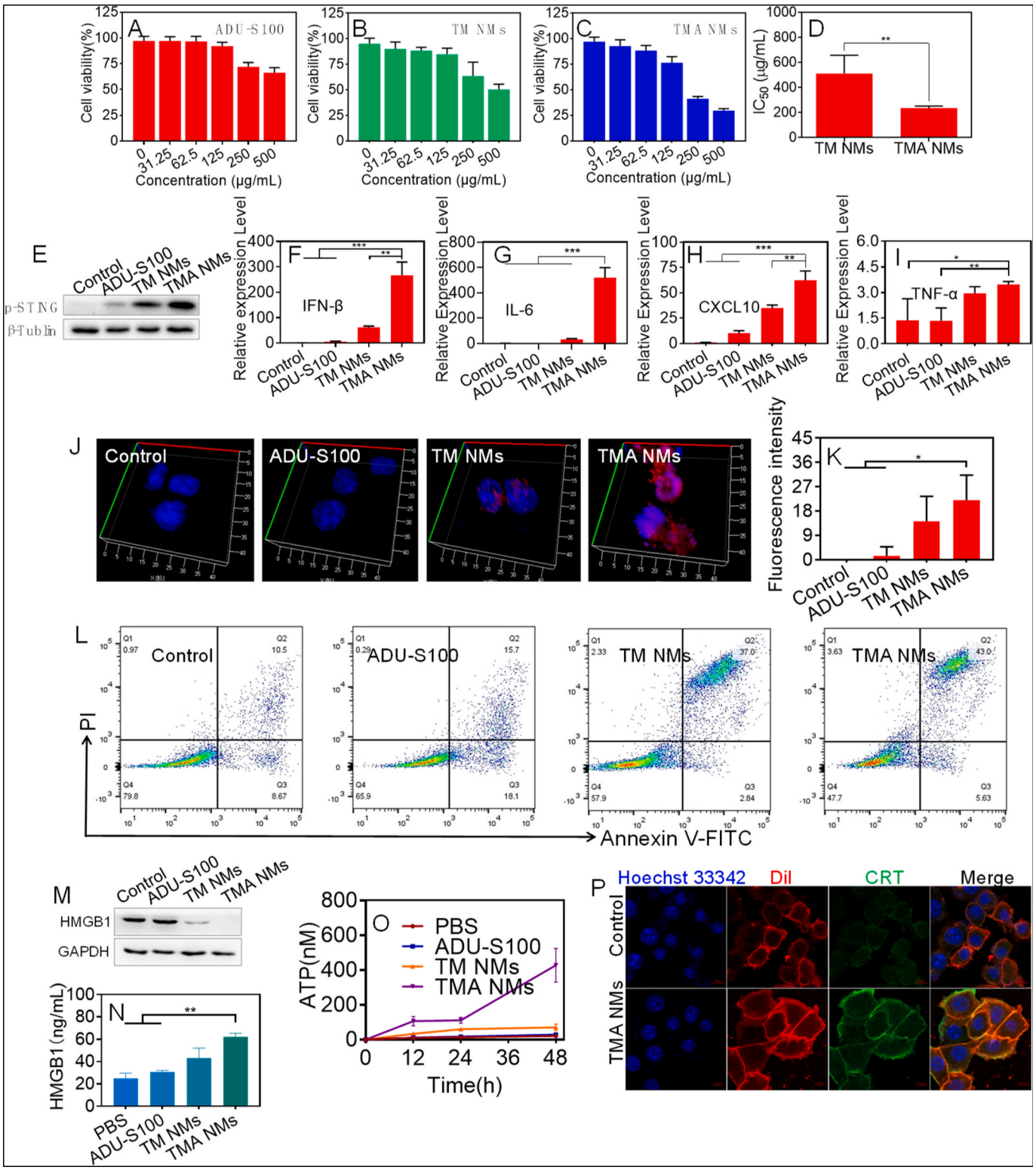

Fig. 2. Cell viability of 4T1 cells following treatment with varying concentrations of (A) ADU-S100, (B) TM NMs, and (C) TMA NMs. (D) IC_{50} values for TM NMs and TMA NMs against 4T1 cells. (E) Western blot analysis of intracellular p-STING expression after varied treatments. Quantitative real-time PCR measuring the gene expression of (F) IFN-β, (G) IL-6, (H) CXCL10, and (I) TNF-α. (J) Assessment of intracellular caspase-3 activity through CLSM imaging after different treatments. (K) Quantitative results of intracellular caspase-3 activity. (L) Flow cytometry analysis of cell death following diverse treatments. (M) Western blot analysis of intracellular HMGB1 expression following different treatments. (N) Levels of HMGB1 secretion following distinct treatments. (O) ATP release in a time-dependent manner following varied treatments. (P) CLSM imaging showcasing CRT expression on 4T1 cell surfaces. The scale bar is 10 μm.

With the anti-tumor mechanism substantiated, we proceeded to investigate the cell death pathways elicited. This was achieved by evaluating the activity of caspase-3, a pivotal protease involved in orchestrating apoptosis, employing a fluorescent Magic Red assay kit. Subsequent to a 48-h incubation, only faint red fluorescence was discernible in cells treated with free ADU-S100 or TM NMs. Significantly, TMA NMs-treated cells exhibited robustly intensified signals (Fig. 2J), indicative of heightened caspase-3 activity, a confirmation that was corroborated through quantification of the fluorescence signals (Fig. 2K), confirming caspase-3-mediated apoptosis. To corroborate these findings, flow cytometry was utilized to analyze cells co-stained with Annexin-V and PI, revealing a heightened level of late-stage apoptosis in TMA NMs-treated cells (Fig. 2L).

Recent investigations have underscored that the activation of the STING pathway can incite immunogenic cell death (ICD) in select cancer cells, a form of inflammatory cell demise that fosters adaptive anti-

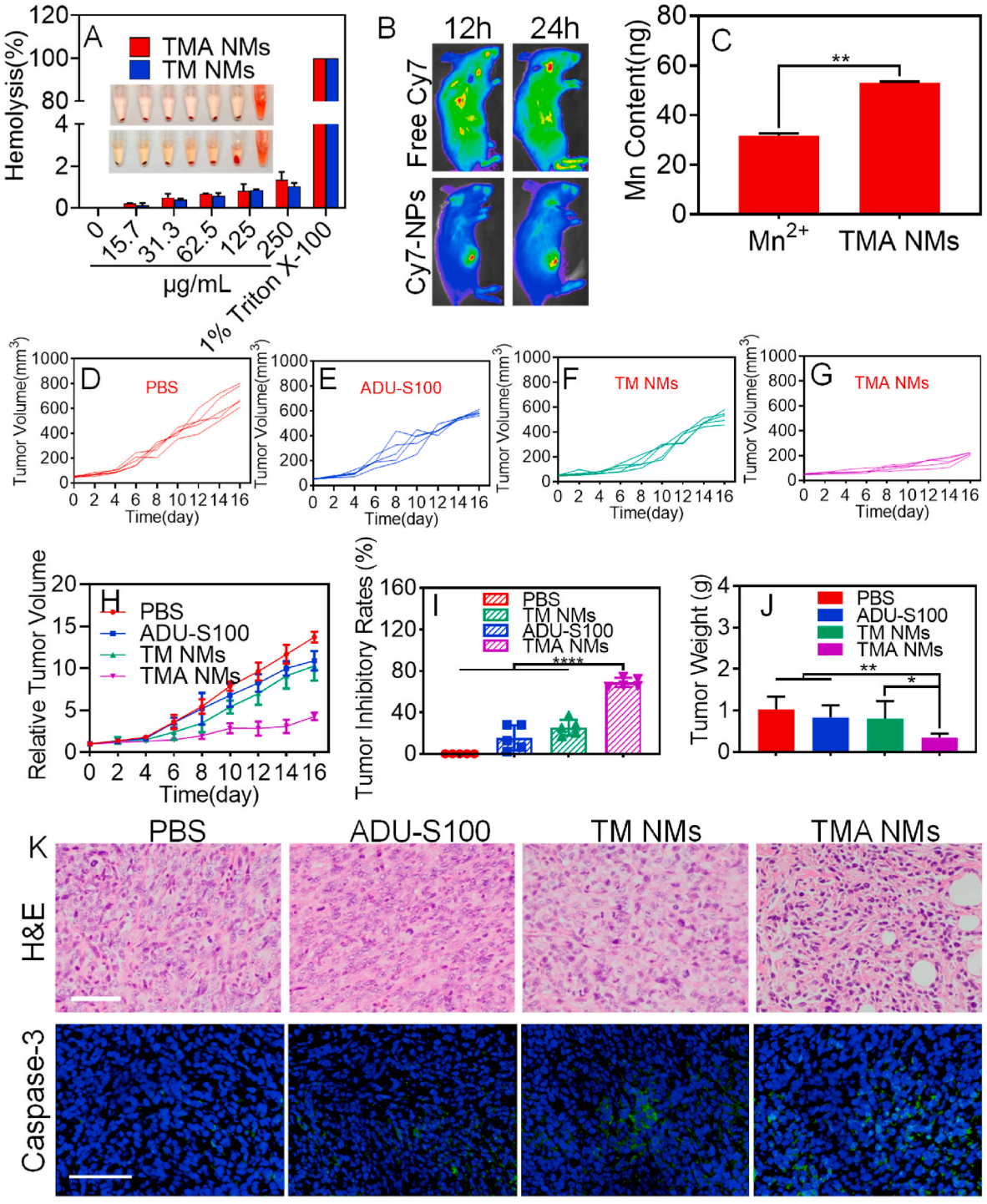

Fig. 3. (A) Hemolysis of TM and TMA at varied concentrations. (B) *In vivo* distribution comparison between free Cy7 and Cy7-labeled NPs. (C) Relative tumor accumulation of Mn at 24 h post-injection. Tumor growth profiles for each mouse post-treatment with (D) PBS, (E) ADU-S100, (F) TM NMs and (G) TMA NMs. (H) Average tumor volume in distinct treatment groups. (I) Tumor inhibitory rates and (J) tumor weight at day 16. (K) Representative histological evaluation through H&E staining and caspase-3 immunofluorescence in tumor tissues following varied treatments. The scale bar is 50 μm and 100 μm for H&E staining and caspase-3 immunofluorescence, respectively.

tumor immunity [47]. We subsequently explored the manifestation of ICD in 4T1 cells by gauging a spectrum of biochemical signals, including the release of HMGB1 and ATP, alongside cell surface expression of calreticulin (CRT). Notably, among the treatment regimens, TMA NMs engendered the lowest intracellular HMGB1 levels coupled with the highest extracellular HMGB1 secretion, underscoring effective HMGB1 secretion (Fig. 2M and N). Furthermore, a time-dependent ATP release was noted (Fig. 2O). Notably, the fluorescent staining of CRT revealed conspicuous cell surface CRT expression post-TMA NMs treatment (Fig. 2P and fig. S8). Collectively, TMA NMs emerged as potent inducers of ICD in tumor cells, prompting the enhanced release of HMGB1 and ATP to stimulate adaptive anti-tumor immune responses, while the surface CRT expression delivered a "eat me" signal to antigen-presenting cells.

3.3. *In vivo targeted delivery and antitumor efficacy of TMA NMs*

Subsequently, we delved into the *in vivo* performance of TMA NMs using the 4T1 tumor-bearing murine model. Given the satisfactory hemocompatibility demonstrated by both TM NMs and TMA NMs (Fig. 3A), intravenous injection was selected as the route of nanoparticle administration. To begin, we scrutinized the biodistribution of the nanoparticles, utilizing Cy7-labeled TMA NMs to enable real-time *in vivo* tracking via an imaging system. In comparison to free Cy7, mice receiving Cy7-labeled TMA NMs exhibited robust fluorescence emanating from the tumor site at 12 h post-injection, with fluorescence intensity at the tumor site further intensifying after 24 h (Fig. 3B). This observation signified nanoparticle accumulation within the tumor. To corroborate targeted tumor accumulation, the Mn content in tumors was quantified subsequent to intravenous administration of TMA NMs or an equivalent amount of free Mn^{2+}. Notably, TMA NMs elicited a twofold higher Mn content within tumors (Fig. 3C), thereby substantiating their tumor-targeted accumulation.

To explore the *in vivo* tumor ablation efficacy, mice bearing 4T1 tumors were randomly divided into four groups (5 mice per group) and subjected to intravenous injections of PBS, ADU-S100, TM NMs, or TMA NMs. All treatment regimens were administered every other day for a total of three doses. To gauge therapeutic effectiveness, tumor volumes were measured every alternate day. Under PBS or free ADU-S100 treatment, tumors exhibited rapid growth, albeit with negligible tumor suppression attributed to the limited impact of ADU-S100 (Fig. 3D and E). The subdued efficacy of ADU-S100 could be attributed to its rapid metabolic clearance during circulation. During TM NMs treatment, an initial degree of tumor growth inhibition was observed (Fig. 3F), attributable to the Mn^{2+}-mediated anti-tumor response. Notably, TMA NMs yielded markedly superior anti-tumor effects compared to ADU-S100 and TM NMs, leading to significant tumor growth suppression (Fig. 3G and H), culminating in an 70% tumor inhibition ratio after 16 days (Fig. 3I). This outcome highlights the synergistic effect of Mn-based nanocarrier with ADU-S100. Subsequent to the treatment period, mice were sacrificed, and tumor tissues were collected for direct assessment, consistently corroborating the observed anti-tumor trends across different treatment groups (Fig. 3J).

To further validate therapeutic efficacy, tumor tissues were subjected to histopathological examination via hematoxylin and eosin (H&E) staining. Notable nuclear necrosis was evident in TMA NMs treated group. Additionally, fluorescent staining of caspase-3 expression underscored significant cell apoptosis following TMA NMs therapy (Fig. 3K).

3.4. *Anti-tumor mechanism of TMA NMs via systemic immune activation*

Having established the robust anti-tumor efficacy of TMA NMs, our focus shifted to elucidating the underlying mechanism. At the cellular level, we previously demonstrated that TMA NMs can activate the STING pathway, leading to the release of various cytokines. To validate this phenomenon *in vivo*, we quantified the mRNA expression levels of key cytokines including IFN-β, IL-6, CXCL10, and TNF-α. Encouragingly, post-TMA NMs therapy, there was a substantial upregulation of these genes, indicative of the activation of the cascading anti-tumor signaling pathways at the gene level (Fig. 4A–D). This observation was further confirmed through ELISA assays, which showed an augmented release of these cytokines (Fig. 4E–H). These cytokines are well-known drivers of anti-tumor immune responses. To corroborate this, we scrutinized changes in the immune microenvironment. In the control group, tumor tissues displayed a low CD86 signal (Fig. 4I), while showing high CD206 signal (Fig. 4J), indicating an immune-suppressive microenvironment with predominant M2 polarization of macrophages. However, treatments led to an increase in CD86 signal alongside a reduction in CD206 signal, indicative of a shift from M2 to M1 macrophage repolarization. Remarkably, TMA NMs exhibited the most pronounced impact. In parallel, we assessed the maturation of dendritic cells (DCs) through the detection of $CD11+CD86^{+}$ dual-positive cells, revealing a similar trend. Notably, TMA NMs exhibited the most potent ability to promote DC maturation (Fig. 4K). Leveraging the polarization of M1 macrophages and maturation of DCs, we evaluated T cell infiltration, the ultimate effectors of anti-tumor immunity. T cells must traffic and infiltrate tumor tissues before recognizing and killing tumor cells. The most notable increase was observed in the levels of $CD8^{+}$ T cells, $CD8^{+}$ IFN-γ+ T cells, and $CD4^{+}$ IFN-γ+ T cells following TMA NMs treatment (Fig. 4L-N), likely due to excretion of CXCL10 to promote CTL trafficking and infiltration. Collectively, these findings underscored the pivotal role of effective systemic immune activation as a fundamental mechanism behind TMA NMs' anti-tumor efficacy. This immune activation was achieved through the STING pathway activation. Specifically, STING pathway activation not only induced immunogenic cell death in tumor cells but also facilitated the release of various cytokines, which synergistically activated anti-tumor immune responses. Hence, delivering STING agonists through Mn-based carriers emerges as a potent avenue for tumor immunotherapy.

3.5. *Biosafety assessment*

To comprehensively ascertain the biosafety of TMA NMs, we conducted a thorough evaluation. The monitoring of body weight alterations during the treatment period serves as a direct indicator of the overall health status of the mice. Notably, over the course of 16 days of treatment, no substantial deviations in body weight were observed (fig. S9), thus attesting to the absence of acute toxicity associated with TMA NMs. Furthermore, we assessed blood biochemical indices, including alanine aminotransferase (ALT), aspartate aminotransferase (AST), creatinine (CRE), blood urea nitrogen (BUN), and creatine kinase MB (CK-MB), after the treatments. In comparison to the control group, all treated mice exhibited normal levels of these biochemical markers (Fig. 5A–E), thereby signifying a dearth of systemic toxicity. Complementing these findings, we subjected the major organs to H&E staining, revealing an absence of pathological alterations (Fig. 5F). Moreover, we quantified the Mn content post-treatment, revealing a significant reduction in Mn concentration at 16 days post-therapy (Fig. 5G). This outcome underscores the effective excretion of Mn from the mice's bodies. Consequently, the Mn-coordinated nanocarrier exhibited both biocompatibility and biodegradability *in vivo*, rendering it highly suitable for diverse biomedical applications.

4. Conclusion

In conclusion, this study provides a comprehensive investigation of TMA NMs as carriers for ADU-S100 to enhance tumor immunotherapy. The synthesized TMA NMs, comprising TA and Mn^{2+}, demonstrated effective encapsulation of ADU-S100, ensuring stability and intracellular responsiveness. Through *in vitro* and *in vivo* experiments, the potential of TMA NMs was validated. The findings revealed that TMA NMs

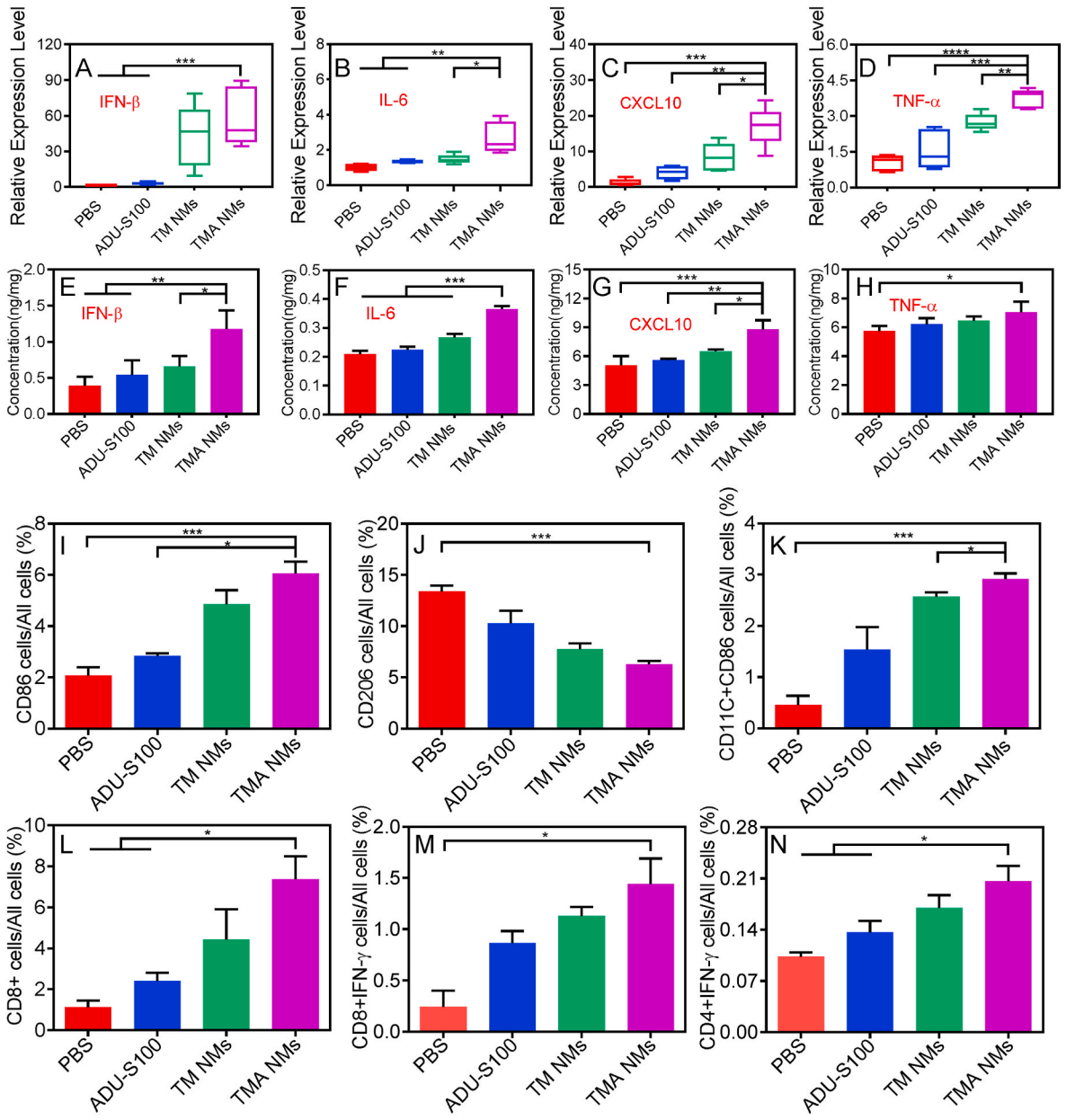

Fig. 4. Gene expression levels of (A) IFN-β, (B) IL-6, (C) CXCL10, and (D) TNF-α within tumor tissues post-distinct treatments. Levels of (E) IFN-β, (F) IL-6, (G) CXCL10, and (H) TNF-α within tumor tissues post-varied treatments. Percentage of (I) CD86, (J) CD206, (K) CD11C + CD86, (L) $CD8^+$, (M) $CD8^+$ IFN-γ+, and (N) $CD4^+$ IFN-γ+ cells within tumor tissues following diverse treatments.

efficiently delivered ADU-S100, leading to the activation of the STING pathway and induction of immunogenic cell death (ICD). This activation resulted in the release of critical cytokines, ultimately leading to significant tumor suppression. Notably, TMA NMs also triggered systemic immune responses, including dendritic cell maturation, polarization of macrophages towards an M1 phenotype, and increased infiltration of cytotoxic T cells into tumor tissues. These synergistic processes collectively contributed to enhanced anti-tumor effects. Importantly, the biosafety assessment demonstrated the biocompatibility and biodegradability of TMA NMs *in vivo*, confirming their potential for biomedical applications. Overall, the results establish TMA NMs as a promising strategy to enhance cancer immunotherapy by addressing delivery challenges and optimizing STING agonist activity, ultimately improving therapeutic outcomes.

CRediT authorship contribution statement

Yingcai Meng: Writing – review & editing, Writing – original draft, Validation, Software, Methodology, Investigation, Funding acquisition, Formal analysis, Data curation. **Jiaxin Huang:** Validation, Investigation, Data curation. **Jinsong Ding:** Resources, Methodology. **Haiyan Zhou:** Writing – review & editing, Supervision, Resources, Methodology. **Yong Li:** Writing – review & editing, Supervision, Resources, Funding acquisition. **Wenhu Zhou:** Writing – review & editing, Supervision, Resources, Funding acquisition, Conceptualization.

Declaration of competing interest

The authors declare that they have no known competing financial interests or personal relationships that could have appeared to influence the work reported in this paper.

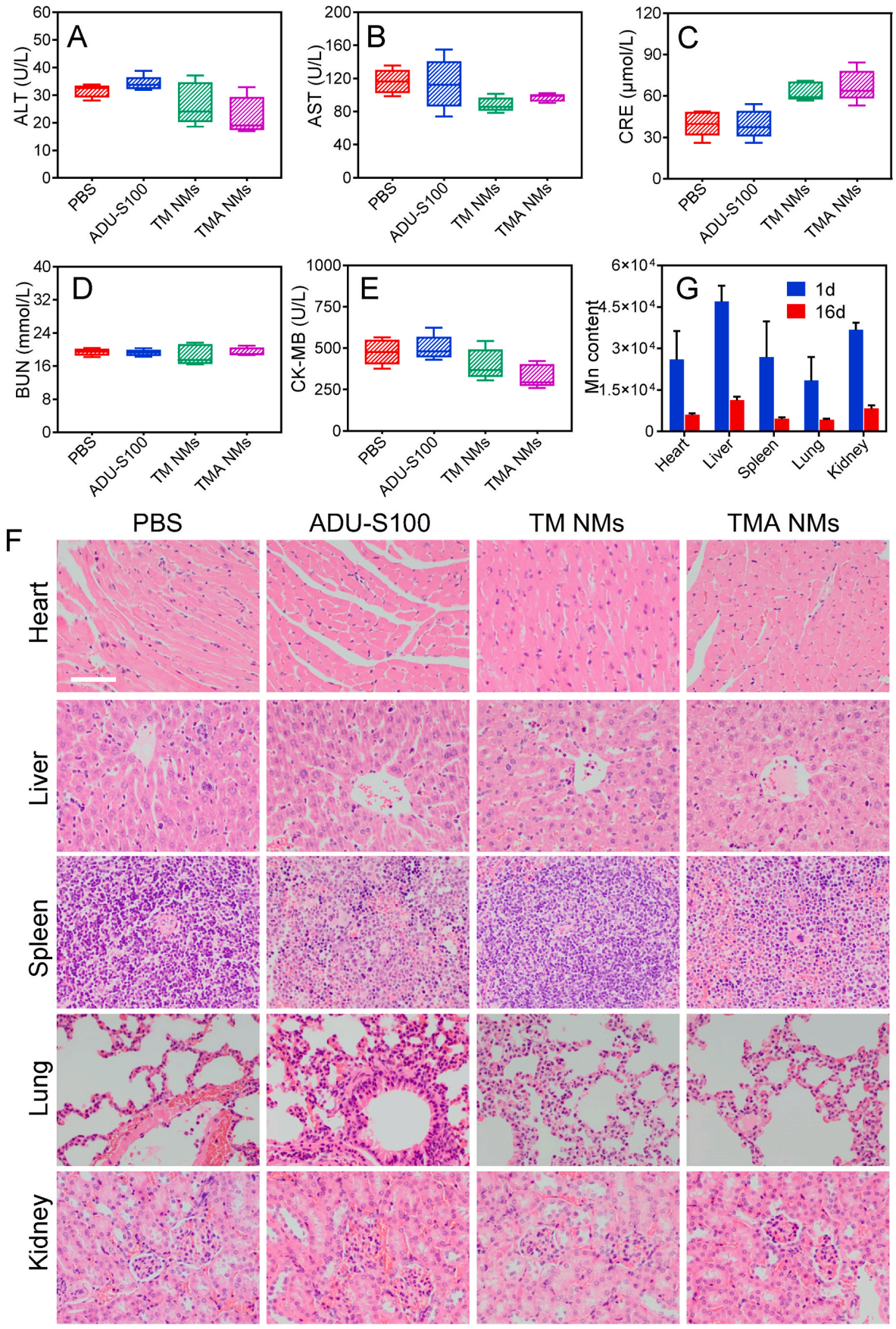

Fig. 5. Serum levels of (A) ALT, (B) AST, (C) CRE, (D) BUN, and (E) CK-MB in mice following varied treatments. (F) Representative histological examination through H&E staining of major organs following diverse treatments. The scale bar is 50 μm. (G) Relative Mn content at day 1 and day 16 post-TMA NMs injection.

Data availability

Data will be made available on request.

Acknowledgments

This work was supported by Natural Science Foundation of Hunan province in China (No. 2021JJ20084, 2022JJ40581, 2023JJ30323), and the Science and Technology Innovation Program of Hunan Province (No. 2021RC3020), the Project Funded by China Postdoctoral Science Foundation (No. 2021M693576), Clinical Research Center For Children's Solid Tumor In Hunan Province, and Hunan Province Health and Family Planning High-level Talent Program.

Appendix A. Supplementary data

Supplementary data to this article can be found online at https://doi.org/10.1016/j.mtbio.2024.101018.

References

[1] M.S. Goldberg, Improving cancer immunotherapy through nanotechnology, Nat. Rev. Cancer 19 (10) (2019) 587–602.
[2] J.D. Martin, H. Cabral, T. Stylianopoulos, R.K. Jain, Improving cancer immunotherapy using nanomedicines: progress, opportunities and challenges, Nat. Rev. Clin. Oncol. 17 (4) (2020) 251–266.
[3] M. Binnewies, E.W. Roberts, K. Kersten, V. Chan, D.F. Fearon, M. Merad, L. M. Coussens, D.I. Gabrilovich, S. Ostrand-Rosenberg, C.C. Hedrick, R. H. Vonderheide, M.J. Pittet, R.K. Jain, W. Zou, T.K. Howcroft, E.C. Woodhouse, R. A. Weinberg, M.F. Krummel, Understanding the tumor immune microenvironment (TIME) for effective therapy, Nat. Med. 24 (5) (2018) 541–550.
[4] P.S. Hegde, D.S. Chen, Top 10 challenges in cancer immunotherapy, Immunity 52 (1) (2020) 17–35.
[5] J.B.A.G. Haanen, Converting cold into hot tumors by combining immunotherapies, Cell 170 (6) (2017) 1055–1056.
[6] I. Vitale, E. Shema, S. Loi, L. Galluzzi, Intratumoral heterogeneity in cancer progression and response to immunotherapy, Nat. Med. 27 (2) (2021) 212–224.
[7] J. Shen, M. Lin, M. Ding, N. Yu, C. Yang, D. Kong, H. Sun, Z. Xie, Tumor immunosuppressive microenvironment modulating hydrogels for second near-infrared photothermal-immunotherapy of cancer, Mater, Today Bio 16 (2022) 100416.
[8] S. Guo, Y. Yao, Y. Tang, Z. Xin, D. Wu, C. Ni, J. Huang, Q. Wei, T. Zhang, Radiation-induced tumor immune microenvironments and potential targets for combination therapy, Sig. Transduct. Target. Ther. 8 (1) (2023) 205.
[9] Y.R. Murciano-Goroff, A.B. Warner, J.D. Wolchok, The future of cancer immunotherapy: microenvironment-targeting combinations, Cell Res. 30 (6) (2020) 507–519.
[10] T. Tang, X. Huang, G. Zhang, Z. Hong, X. Bai, T. Liang, Advantages of targeting the tumor immune microenvironment over blocking immune checkpoint in cancer immunotherapy, Sig, Transduct. Target. Ther. 6 (1) (2021) 205.
[11] O. Demaria, S. Cornen, M. Daeron, Y. Morel, R. Medzhitov, E. Vivier, Harnessing innate immunity in cancer therapy, Nature 574 (7776) (2019) 45–56.
[12] A. Li, M. Yi, S. Qin, Y. Song, Q. Chu, K. Wu, Activating cGAS-STING pathway for the optimal effect of cancer immunotherapy, J. Hematol. Oncol. 12(1) (2019) 35.
[13] J. Wu, L. Sun, X. Chen, F. Du, H. Shi, C. Chen, Z.J. Chen, Cyclic GMP-AMP is an endogenous second messenger in innate immune signaling by cytosolic DNA, Science 339 (6121) (2013) 826–830.
[14] L. Sun, J. Wu, F. Du, X. Chen, Z.J. Chen, Cyclic GMP-AMP synthase is a cytosolic DNA sensor that activates the type I interferon pathway, Science 339 (6121) (2013) 786–791.
[15] D.L. Burdette, K.M. Monroe, K. Sotelo-Troha, J.S. Iwig, B. Eckert, M. Hyodo, Y. Hayakawa, R.E. Vance, STING is a direct innate immune sensor of cyclic di-GMP, Nature 478 (7370) (2011) 515–518.
[16] S.-R. Woo, M.B. Fuertes, L. Corrales, S. Spranger, M.J. Furdyna, M.Y.K. Leung, R. Duggan, Y. Wang, G.N. Barber, K.A. Fitzgerald, M.-L. Alegre, T.F. Gajewski, STING-dependent cytosolic DNA sensing mediates innate immune recognition of immunogenic tumors, Immunity 41 (5) (2014) 830–842.
[17] M. Motwani, S. Pesiridis, K.A. Fitzgerald, DNA sensing by the cGAS-STING pathway in health and disease, Nat. Rev. Genet. 20 (11) (2019) 657–674.
[18] L. Corrales, L.H. Glickman, S.M. McWhirter, D.B. Kanne, K.E. Sivick, G.E. Katibah, S.-R. Woo, E. Lemmens, T. Banda, J.J. Leong, K. Metchette, T.W. Dubensky Jr., T. F. Gajewski, Direct activation of STING in the tumor microenvironment leads to potent and systemic tumor regression and immunity, Cell Rep. 11 (7) (2015) 1018–1030.
[19] Q. Li, M. Yang, X. Sun, Q. Wang, B. Yu, A. Gong, M. Zhang, F. Du, NIR responsive nanoenzymes via photothermal ablation and hypoxia reversal to potentiate the STING-dependent innate antitumor immunity, Mater. Today Bio 19 (2023) 100566.
[20] C. Ding, Z. Song, A. Shen, T. Chen, A. Zhang, Small molecules targeting the innate immune cGAS-STING-TBK1 signaling pathway, Acta Pharm. Sin. B 10 (12) (2020) 2272–2298.
[21] P. Gao, M. Ascano, T. Zillinger, W. Wang, P. Dai, A.A. Serganov, B.L. Gaffney, S. Shuman, R.A. Jones, L. Deng, G. Hartmann, W. Barchet, T. Tuschl, D.J. Patel, Structure-function analysis of STING activation by c G(2′,5′) pA(3′,5′)p and targeting by antiviral DMXAA, Cell 154 (4) (2013) 748–762.
[22] C. Huang, N. Shao, Y. Huang, J. Chen, D. Wang, G. Hu, H. Zhang, L. Luo, Z. Xiao, Overcoming challenges in the delivery of STING agonists for cancer immunotherapy: a comprehensive review of strategies and future perspectives, Mater. Today Bio 23 (2023) 100839.
[23] X. Zhang, Y. Yang, J. Li, X. Xie, Y. Hao, Y. Zhu, Z. Zhang, J. Fu, H. Ma, Engineered oxygen factories synergize with STING agonist to remodel tumor microenvironment for cancer immunotherapy, Adv. Funct. Mater. 33 (2023) 2300833.
[24] H. Zheng, B. Guo, X. Qiu, Y. Xia, Y. Qu, L. Cheng, F. Meng, Z. Zhong, Polymersome-mediated cytosolic delivery of cyclic dinucleotide STING agonist enhances tumor immunotherapy, Bioact. Mater. 16 (2022) 1–11.
[25] K.E. Sivick, A.L. Desbien, L.H. Glickman, G.L. Reiner, L. Corrales, N.H. Surh, T. E. Hudson, U.T. Vu, B.J. Francica, T. Banda, G.E. Katibah, D.B. Kanne, J.J. Leong, K. Metchette, J.R. Bruml, C.O. Ndubaku, J.M. McKenna, Y. Feng, L. Zheng, S. L. Bender, C.Y. Cho, M.L. Leong, A. van Elsas, T.W. Dubensky Jr., S.M. McWhirter, Magnitude of therapeutic STING activation determines CD8+ T cell-mediated anti-tumor immunity, Cell Rep. 25 (11) (2018) 3074–3085.
[26] F. Meric-Bernstam, S.K. Sandhu, O. Hamid, A. Spreafico, S. Kasper, R. Dummer, T. Shimizu, N. Steeghs, N. Lewis, C.C. Talluto, S. Dolan, A. Bean, R. Brown, D. Trujillo, N. Nair, J.J. Luke, Phase Ib study of MIW815 (ADU-S100) in combination with spartalizumab (PDR001) in patients (pts) with advanced/metastatic solid tumors or lymphomas, J. Clin. Oncol. 37 (15) (2019) 2507, 2507.
[27] F. Meric-Bernstam, R.F. Sweis, F.S. Hodi, W.A. Messersmith, R.H.I. Andtbacka, M. Ingham, N. Lewis, X. Chen, M. Pelletier, X. Chen, J. Wu, S.M. McWhirter, T. Mueller, N. Nair, J.J. Luke, Phase I dose-escalation trial of MIW815 (ADU-S100), an intratumoral STING agonist, in patients with advanced/metastatic solid tumors or lymphomas, Clin. Cancer Res. 28 (4) (2022) 677–688.
[28] Y. Wang, J. Luo, A. Alu, X. Han, Y. Wei, X. Wei, cGAS-STING pathway in cancer biotherapy, Mol. Cancer 19 (1) (2020) 136.
[29] T. Lioux, M.-A. Mauny, A. Lamoureux, N. Bascoul, M. Hays, F. Vernejoul, A.-S. Baudru, C. Boularan, J. Lopes-Vicente, G. Qushair, G. Tiraby, Design, synthesis, and biological evaluation of novel cyclic adenosine-inosine monophosphate (cAIMP) analogs that activate stimulator of interferon genes (STING), J. Med. Chem. 59 (22) (2016) 10253–10267.
[30] X. Xie, J. Liu, X. Wang, Design, synthesis and biological evaluation of (2′,5′ and 3′5′-linked) cGAMP analogs that activate stimulator of interferon genes (STING), Molecules 25 (22) (2020) 5285.
[31] N. Ji, M. Wang, C. Tan, Liposomal delivery of MIW815 (ADU-S100) for potentiated STING activation, Pharmaceutics 15 (2) (2023) 638.
[32] S. Song, P. Peng, Z. Tang, J. Zhao, W. Wu, H. Li, M. Shao, L. Li, C. Yang, F. Duan, M. Zhang, J. Zhang, H. Wu, C. Li, X. Wang, H. Wang, Y. Ruan, J. Gu, Decreased expression of STING predicts poor prognosis in patients with gastric cancer, Sci. Rep. 7 (2017) 39858.
[33] Z. Lin, Y. Liu, P. Lin, J. Li, J. Gan, Clinical significance of STING expression and methylation in lung adenocarcinoma based on bioinformatics analysis, Sci. Rep. 12 (1) (2022) 13951.
[34] X. Sun, Y. Zhang, J. Li, K.S. Park, K. Han, X. Zhou, Y. Xu, J. Nam, J. Xu, X. Shi, L. Wei, Y.L. Lei, J.J. Moon, Amplifying STING activation by cyclic dinucleotide-manganese particles for local and systemic cancer metalloimmunotherapy, Nat. Nanotechnol. 16 (11) (2021) 1260–1270.
[35] R. Zhang, C. Wang, Y. Guan, X. Wei, M. Sha, M. Yi, M. Jing, M. Lv, W. Guo, J. Xu, Y. Wan, X.-M. Jia, Z. Jiang, Manganese salts function as potent adjuvants, Cell. Mol. Immunol. 18 (5) (2021) 1222–1234.
[36] C. Wang, Y. Guan, M. Lv, R. Zhang, Z. Guo, X. Wei, X. Du, J. Yang, T. Li, Y. Wan, X. Su, X. Huang, Z. Jiang, Manganese increases the sensitivity of the cGAS-STING pathway for double-stranded DNA and is required for the host defense against DNA viruses, Immunity 48 (4) (2018) 675–688.
[37] M. Ou, C. Lin, Y. Wang, Y. Lu, W. Wang, Z. Li, W. Zeng, X. Zeng, X. Ji, L. Mei, Heterojunction engineered bioactive chlorella for cascade promoted cancer therapy, J. Control. Release 345 (2022) 755–769.
[38] M. Yu, J. Yu, Y. Yi, T. Chen, L. Yu, W. Zeng, X.-k. Ouyang, C. Huang, S. Sun, Y. Wang, Y. Liu, C. Lin, M. Wu, L. Mei, Oxidative stress-amplified nanomedicine for intensified ferroptosis-apoptosis combined tumor therapy, J. Control. Release 347 (2022) 104–114.
[39] R.A. Mustafa, M. Ran, Y. Wang, J. Yan, Y. Zhang, J.M. Rosenholm, H. Zhang, A pH/temperature responsive nanocomposite for chemo-photothermal synergistic cancer therapy, Smart Materials in Medicine 4 (2023) 199–211.
[40] J. Zhai, H. Yang, Z. Wang, Y. Li, C. Ning, Multifunctional nanomaterials-enhanced synergistic son-phototherapy: breaking the limitation of monotherapy, Smart Materials in Medicine 3 (2022) 315–328.
[41] H. Zhu, C. Yang, A. Yan, W. Qiang, R. Ruan, K. Ma, Y. Guan, J. Li, Q. Yu, H. Zheng, L. Tu, S. Liu, Z. Dai, Y. Sun, Tumor-targeted nano-adjuvants to synergize photomediated immunotherapy enhanced antitumor immunity, View 4 (3) (2023) 20220067.
[42] J. Guo, Y. Ping, H. Ejima, K. Alt, M. Meissner, J.J. Richardson, Y. Yan, K. Peter, D. von Elverfeldt, C.E. Hagemeyer, F. Caruso, Engineering multifunctional capsules through the assembly of metal-phenolic networks, Angew. Chem., Int. Ed. 53 (22) (2014) 5546–5551.

[43] M. Fan, Y. Liu, Y. Ren, L. Gan, Y. Yang, H. Wang, Y. Liao, X. Yang, C. Zheng, Q. Wang, Cascade reaction of "Mn^{2+} -catechol" triggered by H_2O_2 to integrate firm tumor vessel embolization and hypoxic response relief, Adv. Healthc. Mater. 11 (15) (2022) e2200544.
[44] Y. Meng, J. Huang, J. Ding, B. Yan, Y. Li, X. Gao, W. Zhou, Poly-thymine DNA templated MnO2 biomineralization as a high-affinity anchoring enabling tumor targeting delivery, J. Colloid Interface Sci. 637 (2023) 441–452.
[45] P. Liu, Y. Zhou, X. Shi, Y. Yuan, Y. Peng, S. Hua, Q. Luo, J. Ding, Y. Li, W. Zhou, A cyclic nano-reactor achieving enhanced photodynamic tumor therapy by reversing multiple resistances, J. Nanobiotechnol. 19 (1) (2021) 149.
[46] P. Liu, X. Xie, M. Liu, S. Hu, J. Ding, W. Zhou, A smart MnO_2-doped graphene oxide nanosheet for enhanced chemo-photodynamic combinatorial therapy via simultaneous oxygenation and glutathione depletion, Acta Pharm. Sin. B 11 (3) (2021) 823–834.
[47] L. Wang-Bishop, M. Wehbe, D. Shae, J. James, B.C. Hacker, K. Garland, P. P. Chistov, M. Rafat, J.M. Balko, J.T. Wilson, Potent STING activation stimulates immunogenic cell death to enhance antitumor immunity in neuroblastoma, J. Immunother. Cancer 8 (1) (2020) e000282.